Diffusion trapped oxygen in oxide derived Copper electrocatalyst in CO_2 reduction

Zan Lian[1]*, Federico Dattila[2] and Núria López[1]*

[1]Institute of Chemical Research of Catalonia (ICIQ), The Barcelona Institute of Science and Technology (BIST), Av. Països Catalans 16, 43007 Tarragona, Spain

[2]Department of Applied Science and Technology (DISAT), Politecnico di Torino, Corso Duca degli Abruzzi 24, 10129, Turin, Italy

*Email: zlian@iciq.es, nlopez@iciq.es

ABSTRACT: Oxide-derived Cu (OD-Cu) catalysts have shown an excellent ability to ensure C-C coupling in the electrochemical carbon dioxide reduction reaction (eCO_2RR). However, these materials extensively rearrange under reaction conditions, thus the nature of the active site remains controversial. Here, we studied the reduction process of OD-Cu *via* large-scale molecular dynamics at first-principles accuracy introducing experimental conditions. The oxygen concentration in the most stable OD-Cu materials increases with the increase of the pH/potential/specific surface area. In long electrochemical experiments, the catalyst would be fully reduced to Cu, but it takes a considerable amount of time to remove all the trapped oxygen, and the highly reconstructed Cu surface provides various sites to adsorb oxygen under relatively stronger reduction potentials (U = –0.58 V_{SHE} at pH=14, 0.25 V_{RHE}). This work provides insight into the evolution of OD-Cu catalysts and residual oxygen during the reaction conditions and a deep understanding of the nature of active sites.

Closing the carbon cycle through electrochemical carbon dioxide reduction (eCO_2R) with renewable energy has attracted attention for its potential to reach net-zero technologies.[1–3] Cu-based catalysts were considered the only class of materials able to perform C-C coupling[4,5] providing valuable C_{2+} products at high reaction rates.[6–11] Cu and particularly oxide-derived Cu (OD-Cu) catalysts exhibit significant structure sensitivity,[12–15] the later produce C_{2+} with higher current density and Faradaic efficiency (F.E. = 45% to 80%) at reasonable overpotentials (U = –0.40 to –1.00 V_{RHE}).[12,16–20] Under the experimental conditions these materials show a highly dynamic behavior with profound stoichiometric and geometric rearrangements.[21–24]

The unique performance of OD-Cu has been attributed to the singularities of its morphology,[18–23] however the real structure under reaction conditions remains controversial[15,16,29–36] due to its highly dynamic behavior under experimental conditions.[31–34] According to XRD and Raman experiments,[31,41] OD-Cu shall be reduced in the bulk according to thermodynamics[42,43], but pulse experiments[16] show that residual oxygen[44,45] can be trapped, enhancing the electrocatalytic process.[46,47] Monodispersed oxide nanoparticles (NPs) reduced under CO_2RR conditions were found to morphologically evolve very rapidly *via* an electrochemical scrambling process, with the initial formation of Cu aggregates that under air exposure conditions change into Cu_2O nanocubes.[6] Moreover, the existence of oxygen species under reductive conditions were investigated by grazing incident hard X-ray photoelectron spectroscopy of OD-Cu prepared by reduction of Cu oxide with H_2 without exposing to air thus being able to extract the oxygen depth distribution profiles.[29] These experiments identify separated Cu_2O buried in the material, oxygen in the lattice close to the surface replacing Cu atomic positions, and O as interstitials in Cu. Computational models have attempted to disentangle such complexity, but have faced similarly severe limitations. Models for fully oxygen depleted models have been investigated in classical Molecular Dynamics[48]. Particularly roughened copper surfaces consisting of 10^6-10^7 atoms created by removing heteroatoms from cuprous oxide, nitride, phosphide, and sulfide[48] with classical effective medium theory reported four types of sites, indicating that over-coordinated 4-fold hollow sites were beneficial to produce C_{2+} species. Alternatively, OD-Cu models were investigated by *Ab Initio* Molecular Dynamics (AIMD)[14] but at fixed oxygen contents, *i.e.* decoupled of the experimental conditions.

Recent developments of neural network potentials derived from massive DFT simulations hold the key for a proper structural and energetic analysis of this long time and extended length OD-Cu dynamic phenomena. A first attempt showing the feasibility of the approach[49] was carried out for an

OD-Cu slab built by removing surface oxygen gradually until no oxygen appears on the surface in 1 ns. A pure Cu surface with the base of Cu_2O was finally formed, and the results show that the planar-square and convex-square sites are selectivity to ethylene. However, the simulations fail to observe the diffusion of oxygen due to the short simulation time and thus did not explain the complete reduction of Cu_2O to Cu observed in many of the experiments.

Both the content and the depth profile of the oxygen distribution is highly contentious since OD-Cu is easily re-oxidized when it is characterized by ex-situ methods limiting experimental capability to assess active and selective ensembles during operation. To gain an insight on the OD-Cu structures in eCO_2RR we trained an accurate neural network potential to address the highly dynamic nature of the catalysts strongly coupled to the history of the sample and to the reaction conditions. Based on the OD-Cu structure, the structure under different conditions and distributions of active sites were obtained paving the way for their control.

Methodological approach

The modeling procedure, Figure 1, fits a Neural Network Potential to simulate OD-Cu systems, to allow long Molecular Dynamics simulations coupled to an external oxygen reservoir to identify the most likely oxygen contents under different experimental conditions. To this end, we have generated a Density Functional theory (DFT PBE-D2[50–53]) initial dataset with the most common Cu, Cu_xO and Cu_2O models, generated by optimizing bulks and surfaces and AIMD simulations.

The Behler-Parrinello high-dimensional neural network potential (HDNNP)[54] was constructed using the neural network potential package (n2p2)[55] on the initial dataset (Figure 1), as described in Methods and Section S1. The NNPs were trained *via* multistream extended Kalman filter algorithm using energies and forces, and the dataset was expanded *via* ***active learning***, Figure 1. In short, two NNPs were trained with the initial dataset. And 1%-25% of structures of the dataset were used to perform the Neural Network based Molecular Dynamics (NN-MD) simulations using one of the NNPs. The NN-MD simulations were performed using LAMMPS[56] code with the NNP interface from n2p2[57]. Upon running NN-MDs with the two NNPs, around one-thousandth structures were collected as seeds for further DFT simulations. These were further selected as follows: (i) one third of structures whose symmetry function values are not within the range of the current dataset (i.e. extrapolations)[58] (ii) by comparison of the two NNPs runs, when the differences between two predictions (energy and forces) are larger than threshold (~5-10 × RMSE). The latter strategy allows identifying structures beyond the

explored structure space as interpolation. Then the dataset was updated with the DFT values for these newly calculated structures. Finally, to ensure the robustness of the potential, NVT simulations for models under extreme conditions (at least 1100 K, 1 ns) were performed. These models include: (i) a Cu slab with 3240 atoms generated by removing all oxygen from an $Cu_2O(111)$ pristine system, (ii) for Cu_2O, a $Cu_{1415}O_{784}$ cluster, and (iii) for Cu_xO, a slab of OD-Cu ($Cu_{444}O_{56}$) from our previous study[14].

To ensure representativity and transferability, the dataset was constructed through two stages. First, the data for Cu and Cu_2O were built *via* active learning separately. Then the intermediate composition structures of Cu_xO were selected. In total, 443 iterations of the active learning process were conducted, in which 8.16×10^{10} steps were ran from NN-MDs, and 8.30×10^{7} structures were compared using two NNPs, and a final dataset with 59491 points was obtained, Table S3. Once trained, the root mean squared error (RMSE) of the energy (force) is 4.58 meV/atom (63.61 meV/Å) on the training set and 4.59 meV/atom (63.48 meV/Å) on test set as shown in Supplementary Section S1.2 and Figure S6. The errors are one order of magnitude smaller than the requirement for chemical accuracy (1 kcal/mol, i.e. 43 meV/atom), which indicates that the NNP has the same level of chemical accuracy as the reference PBE-D2 functional. Similar errors on training and test set indicate no overfitting.

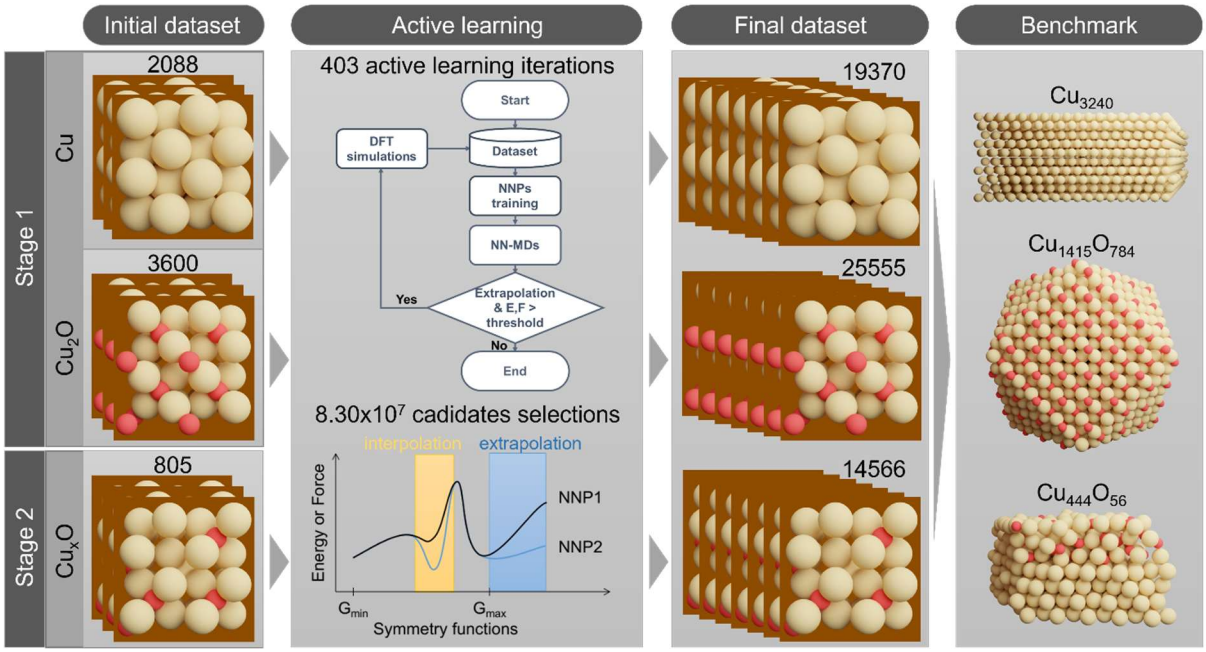

Figure 1. Computational modeling approach for constructing the neural network potential. The data was collected in two stages. In stage 1, the structures of Cu and Cu_2O were selected via the active learning procedure, respectively. Based on the dataset of stage 1, the dataset of Cu_xO was built. In the active learning process, 443 iterations were performed in total, 8.16×10^{10} steps were ran from NN-MDs, and 8.30×10^{7} structures were checked for extrapolation and interpolation. In the end, the final

dataset consists of 59491 points containing 1,801,491 atomic environments and the NNPs are applicable for all three structures.

Results

Thermodynamics of the OD-Cu reduction

To address the thermodynamic fraction of oxygen in OD-Cu under different conditions, we started by a perfect $Cu_2O(111)$ slab to examine the role of pH, electric potential, and specific surface area (S.S.A. = surface/volume), see Figure 2. pH and electric potential were introduced through the Computational Hydrogen Electrode[59]. The O-deficient configurations were simulated by the sequential removal of O atoms. For each step, the same number of oxygen (1/48 of the total number of oxygen in the perfect slab) were random chosen and removed from the previous structure until all oxygen atoms were removed after 48 steps. The thermodynamic minima were identified for each case by using a NN-MD annealing simulation.

Figure 2a shows the free energy of OD-Cu reduction as a function of ***pH***. At low pH, OD-Cu tends to be fully reduced to generate pure copper. While at high pH values, which are typical of highly active and ethylene selective CO_2RR electrolyzers,[60] all the steps of the reduction are endergonic, and the perfect Cu_2O is the most stable state. At intermediate pH, the partially reduced Cu_2O system is the thermodynamic ground state. In electrochemical media, with $KHCO_3$ buffer as electrolyte (pH 6.8-8) about ~15.7 at.% oxygen would remain in a system with a S.S.A. of 0.146 $Å^{-1}$ at zero potential vs SHE. However, the reduction of the first 45.8% (22/48) of oxygen is endergonic, which indicates that starting the reduction requires a driving force. As expected, the driving force can be the ***electric potential***, as shown in Figure 2b, at more reductive potentials, the reduction to copper is favorable. Metallic copper is more favorable than all the partially reduced OD-Cu structures at potential as small as –0.20 V_{SHE} (0.28 V_{RHE}). However, the 'elementary step' with largest positive reaction energy was considered to be the potential limiting step and prevent further reduction. This results in a potential of -0.68 V_{SHE} (-0.20 V_{RHE}) to ensure that all steps are exothermic, indicating OD-Cu reduction is kinetically limited at weak reduction potentials.

To understand size effect on the reduction degree of OD-Cu, slabs of different thicknesses (equivalent to spherical nanoparticles of a diameters between 17.5 and 4.1nm) were simulated. Figure 2c shows that the final state differs significantly. Large nanoparticles keep low oxygen quantities if any, while the smallest one retains 15% of O-atoms, and the overall reaction energy is slightly

endergonic, Table S4. The lower the S.S.A., the larger amount of energy (per atom) is released to reach the same reduction level. On the contrary, the higher the S.S.A., the more oxygen is retained in the most stable structure. This phenomenon can be explained by the lower surface energy of $Cu_2O(111)$ (0.665 J/m^2) compared to Cu(111) (1.339 J/m^2)[61], and the reconstruction of Cu_2O surface could significantly reduce the energy of the system as shown in Section S2.2. This observation is in line with a recent experimental study using Atomic-scale STEM and electron energy loss spectroscopy techniques in which the small Cu nanoparticles were completely oxidized to Cu_2O while the large Cu nanoparticles formed $Cu@Cu_2O$ structures.[6]

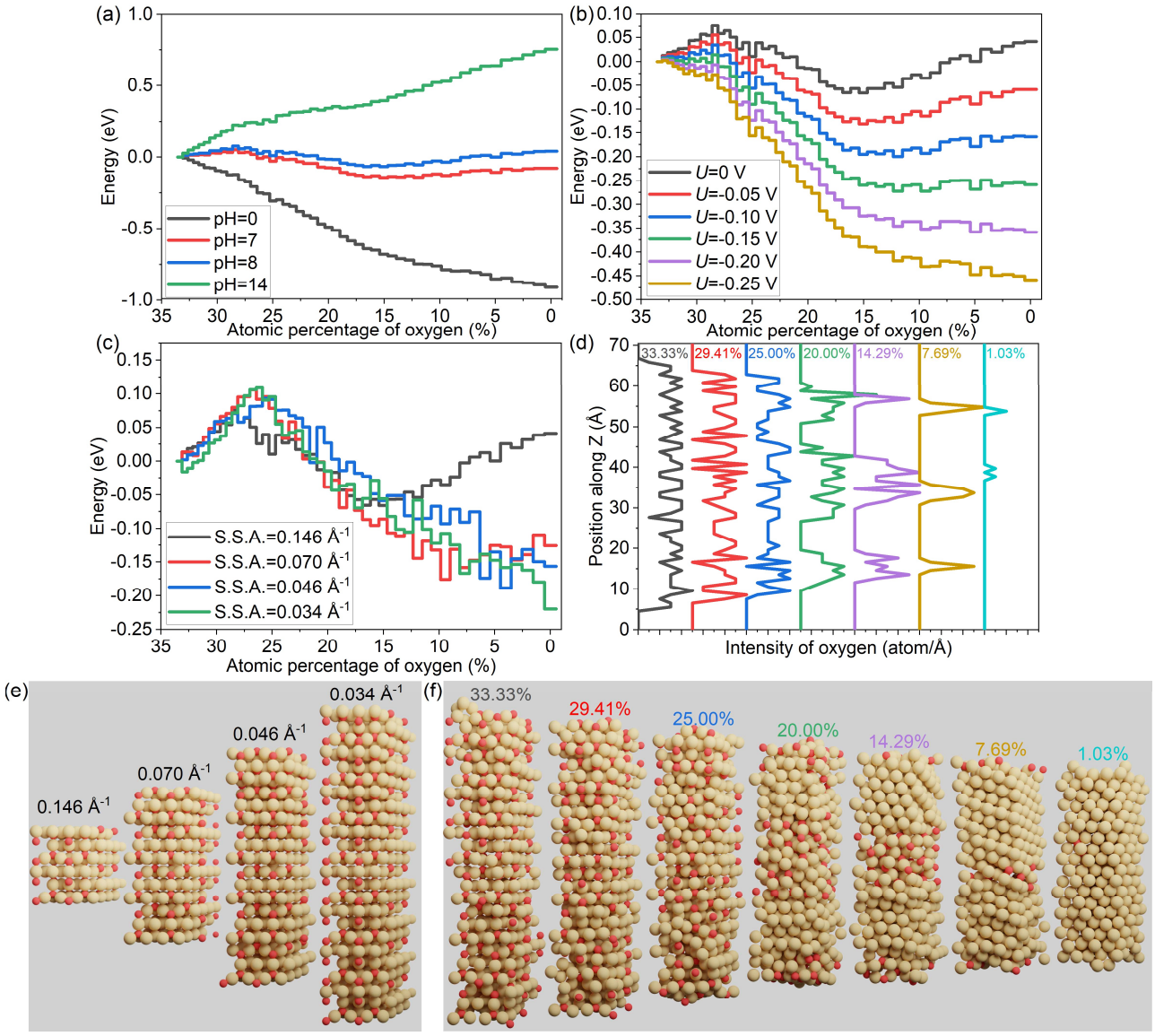

Figure 2. The reduction of Cu_2O to Cu under different conditions. The system (a) under different pH value, at $U = 0$ V_{SHE}, S.S.A. = 0.146$Å^{-1}$, (b) under different electric potential vs SHE, at pH = 8, S.S.A. = 0.146$Å^{-1}$, (c) with different specific surface area, at pH = 8, $U = 0$ V_{SHE}. The reaction energies were calculated from mean energy of OD-Cu in last 800 ps equilibrium in annealing simulations, and

the overall energy was normalized to per unit of Cu_2O. (d) The distribution of oxygen along *z* axis for last frame of OD-Cu (S.S.A. = 0.034Å^{-1}) with different oxygen concentrations. A minor tick interval in horizontal axis is 1 atom/Å, (e) The model of Cu_2O slab with different S.S.A., oxygen in red, copper in brown, (f) The configurations of OD-Cu structures corresponding to (d).

The distribution of oxygen

After annealing, most of the oxygen would be located close to the surface to form the structure of $Cu_2O(111)$ if the remaining number of oxygen atoms fits the capacity of the surface. Still, the reason could be that $Cu_2O(111)$ has lower surface energy than Cu(111), and the formation of Cu_2O on the surface can reduce the energy of the system. But few oxygen atoms could be trapped inside, Figure 2d. If the amount of oxygen atoms exceeds the capacity of the surface, the excess oxygen atoms aggregate in the bulk to form Cu_2O grains, consistent with the experimental results.[29] The oxygen depth profile shown in Figure 2d for the low specific surface area model (S.S.A. = 0.034 Å^{-1}, Figure 2e), shows three peaks corresponding to Cu_2O, two on the surface and one inside the bulk. The peak inside the bulk indicates the formation of a Cu_2O layer (4 atoms per 1.08 Å for $Cu_2O(111)$-p(2×2)) parallel to the surface as Cu_2O has a lower formation energy than Cu_xO (x =1, 6, 8, 64)[14,61]. Therefore, oxygen atoms tend to aggregate to form Cu_2O to reduce the overall formation energy, and near the surface to further reduce the surface energy. Thus, considering a large size OD-Cu catalyst containing enough O, the stable static configuration should be that part of oxygen atoms are located on the surface to form Cu_2O surface. Meanwhile, excess oxygen leads to Cu_2O formed inside the bulk segregated from the Cu crystal.[6,29] The diffusion and aggregation of oxygen were also observed in the NVT simulation at 300 K showed upon long-time equilibration (100 ns), Figure 3a. The two peak inside the bulk at 10 ns correspond to the two types of oxygen proposed by a recent XPS study[29], Figure S7.

The Cu-only crystal structure domains formed either on the surface or inside the bulk can suppress oxygen diffusion. As shown in Figure 3b, when the top six atomic layer oxygen were removed from the initial slab, the remaining Cu atoms collapse immediately, resulting in the formation of a metallic shell on the surface with a similar configuration of face-centered cubic copper. At 300 K, no oxygen atom diffuses to the surface after 100 ns equilibrium (even after 900 ns at 400 K) as shown in Figure 3b. This indicated that the diffusion of oxygen is highly restrained by the dense pure metallic shell. From equilibrium simulations at different temperatures, until the equilibrium temperature increases to 600 K, the diffusion of oxygen from inside to the surface was observed in the equilibration time in

this work, *i.e.*, 1 ns (the first oxygen appears on the topmost layer in 0.72 ns). Although the formation of Cu_2O surface is more favorable, the sluggish kinetics of oxygen diffusion could slow down the process.

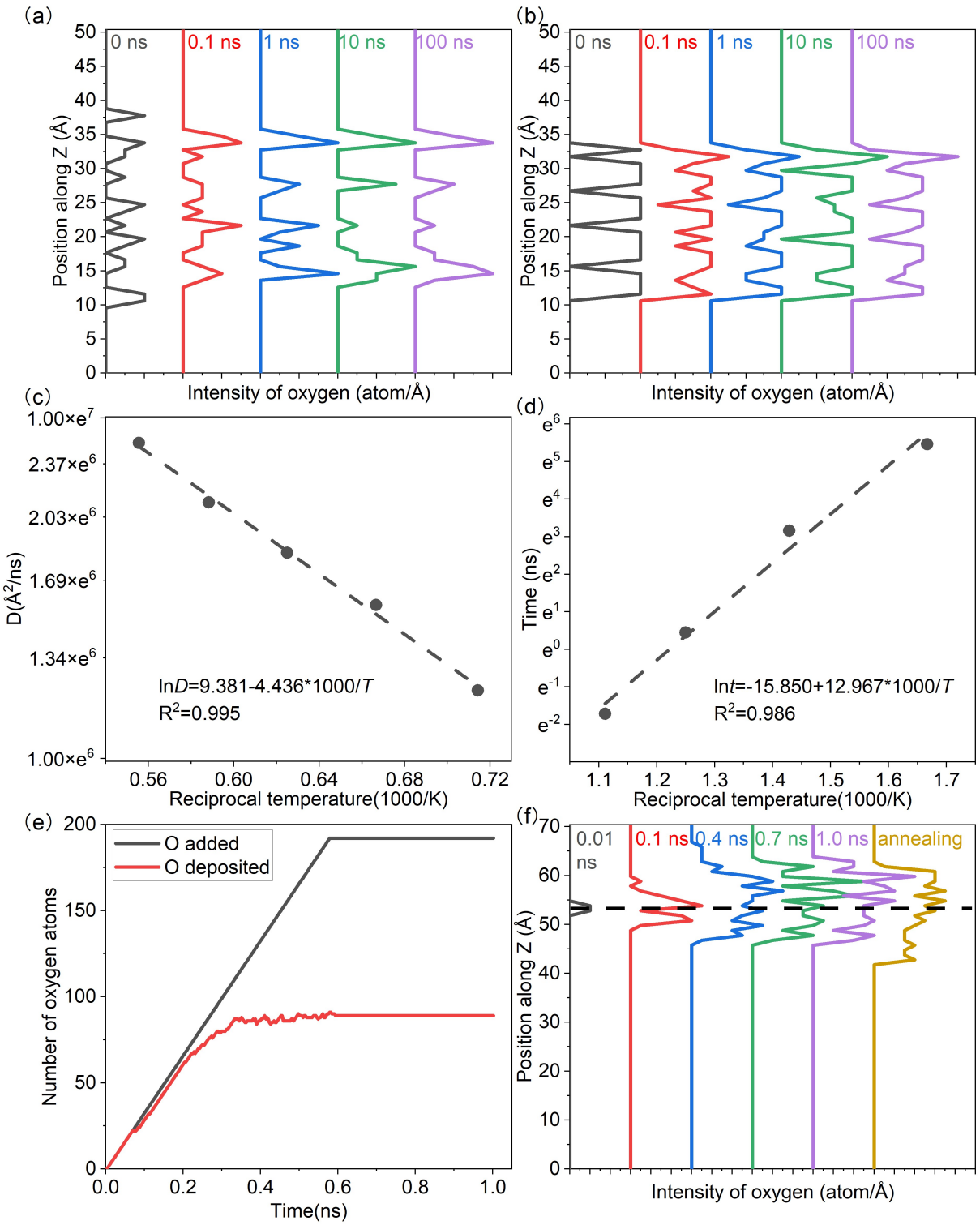

Figure 3. The evolution of oxygen distribution along z axis in OD-Cu during reduction and deposition and oxygen diffusion kinetics relation with temperature. (a) evolution of oxygen

distribution for OD-Cu (9.43 at.% O, the most stable case at S.S.A. = 0.070 $Å^{-1}$, pH = 8, U = 0 V_{SHE}, Figure 2c) created by removing random oxygen atoms, (b) evolution of oxygen distribution for OD-Cu (S.S.A. = 0.070 $Å^{-1}$) created by removing oxygen atoms at top most atomic layers, (c) the relation between temperature and oxygen diffusion coefficient in perfect Cu_2O bulk, (d) the relation between temperature and diffusion time of oxygen from inside to surface in OD-Cu system of (b), (e) the evolution of number of added oxygen atoms and deposited oxygen atoms, (f) oxygen distribution during the deposition, the dashed indicates the surface at 0 ns.

Figure 3c shows the diffusion coefficient of oxygen, D_O, in pristine Cu_2O bulk as obtained from the meaningful[62] data of mean squared displacement (MSD) at high temperatures (1400 K to 1800 K). Using the exponential dependence, the D_O at low temperatures were estimated, 4.5×10^{-3} $Å^2$/ns and 81.6 $Å^2$/ns at 300 K and 900 K respectively. Considering a one-dimensional diffusion with distance of 6 Å, the diffusion time is 0.22 ns under 900 K, 0.92 ns under 700 K, 2.72 ns under 600 K, and 4007.96 ns under 300 K.

To further evaluate the diffusion of oxygen in the Cu shell case, the simulations for the model in Figure 3b were ran for at least 300 ns for 400-800 K (with 100K intervals). Below 500K, no oxygen appears on the surface even after 300ns. Already at 600 K, at most 4 oxygen atoms appear in the run and the last oxygen atom first emerges at 235.7 ns (diffusion distance ~ 6Å), while at 900 K this happens even below ns scale, Table S5.

Additionally, an exponential relation for the diffusion time and temperature was obtained as shown in Figure 3d. The estimated times for 4 oxygen atoms appearing on the surface are 2.40×10^4 ns, 1.56×10^7 ns, and 7.72×10^{11} ns (772 s ≈ 0.2 h) at 500 K, 400 K, and 300 K, respectively. From the relation, at 300K, the diffusion time for 3.5 nm is 7.3 h. The diffusion of oxygen is greatly constrained in the latter case, thus difficult to be observed in the time scale of simulations but certainly can occur on the time scale of the experiment.

The re-oxidation of reduced OD-Cu

To reproduce exhibition to air or a pulsed potential we have employed the reduced OD-Cu systems in the re-oxidation process by depositing oxygen atoms at 300 K on pure Cu reconstructed slab obtained in Figure 2f system. The initial model has 384 Cu atoms and to reach the conversion to Cu_2O, 192 oxygen atoms were gradually added to the system at a rate of 1 atom per 3 ps, and initial velocity of 1

Å/ps from 3 Å above the surface atom to avoid the high-speed collision. Initially the oxygen atoms are adsorbed on the surface, and at about 0.06 ns, all the 20 adatoms are sit on the surface. As the content increases, most of the oxygen (103/172) from the deposition source cannot reach the surface due to the repulsion with the surface oxygen. However, after a short time (0.1 ns from the start), the copper atoms are dragged by the surface oxygen, forming a loose structure that allows to accommodate more oxygen atoms, simultaneously some oxygen atoms penetrate deeper into the bulk. After 89 oxygen atoms oxidize the material, the process stops (Figure 3e). Additional simulation gives the same results even adding 300 oxygen atoms into the system (Figure S8). The final thickness of the oxide layer is 16.9 Å (Figure 3f, 46.3 Å to 63.2 Å), in which 6.9 Å of oxide copper are below the original surface (dashed line in Figure 3f, 53.2 Å), and 10 Å above the original surface, the former indicating the diffusion of oxygen to the interior and the latter corresponding to the outward displacement of Cu. This agrees with the experimental result that only the near surface layers are oxidic[38]. Unlike in the reduction process, where the oxygen diffusion from inside to surface was not observed under 300 K when dense copper formed on the surface, here, in the oxidation simulation the oxygen rapidly diffuses from the surface to 6.9 Å inside the surface. The reason may be that copper has enough space to move on the surface. Again, when the oxygen diffuses to 6.9 Å under the surface, the dense copper prevents the diffusion of oxygen, in conjunction with difficulty of depositing more oxygen to the surface, and deep oxidation takes longer.

In addition, the component of oxide layers (atoms above the deepest oxygen) on the surface is $Cu_{79}O_{89}$ ($Cu_{71}O_{89}$ for the 300 atoms case), indicating that the surface Cu is mainly Cu(II). After annealing, the component changes to $Cu_{112}O_{89}$ ($Cu_{139}O_{89}$ for the 300 atoms case) which is Cu(II) and Cu(I) and the thickness changes from 17 Å to 21 Å, which is comparable to the experimental findings (2∼3 nm)[6,29,38].

The active site via graph theory

Considering typical experimental settings, a Cu_2O nanoparticle with the diameter of 20 nm[37], at pH 8 and U = –0.3 V_{RHE}, should be reduced to pure Cu. To simulate the high roughness of the surface, a 3240 atom Cu slab derived by removing all oxygen from a 30 atomic layers Cu_2O(111)-p(9×9) was used. After equilibrium, the slab structure (equivalent to 4.4 nm NP) forms a loss configuration with average coordination number (with a decay controlled by an error function[14]) of 9.08. 2861 active sites are detected via Delaunay triangulation sampling[63] of the last frame of the simulation, and there are

16 unique active sites based on the isomorphism analysis[64] as shown in Figure 4a. The last 9 unique active sites together represent only 0.45% of the number of total active sites, thus they are categorized to 1 class (H) for analysis. Therefore, 8 classes of active sites are considered. A, B, and C categories account for the most, 13.28%, 49.98%, and 27.19% populations, corresponding to atop, fcc/hcp, and bridge sites, respectively, and the Cu atoms in these sites could be under-coordinated. Class F (2.48%) also represents three coordinated sites, but unlike the hcp/fcc sites, two of the Cu atoms are not interconnected. D(4.89%), E(1.12%), and G(0.59%) categories represent four coordinated sites, where E is similar to the hollow site on (100), while the other two categories are connected in different ways.

The reconstructed surface gives a wide distribution of oxygen desorption energies from –0.51 eV to –3.10 eV at pH 0, $U = 0$ V_{SHE}. At pH 8, $U = 0$ V_{SHE}, 25.2% of the oxygen desorption is endoergic, and all the oxygen would be removed from the surface at reduction potentials more negative than –0.22 V_{SHE} (0.26 V_{RHE}). Instead, at pH 14, the reduction potential needs to be lower than –0.58 V_{SHE} (0.26 V_{RHE}) to completely remove the residual oxygen. Thus, the residual oxygen on the surface can exist under certain experimental conditions and the amount of residual oxygen could be finely tuned by controlling the reaction conditions.

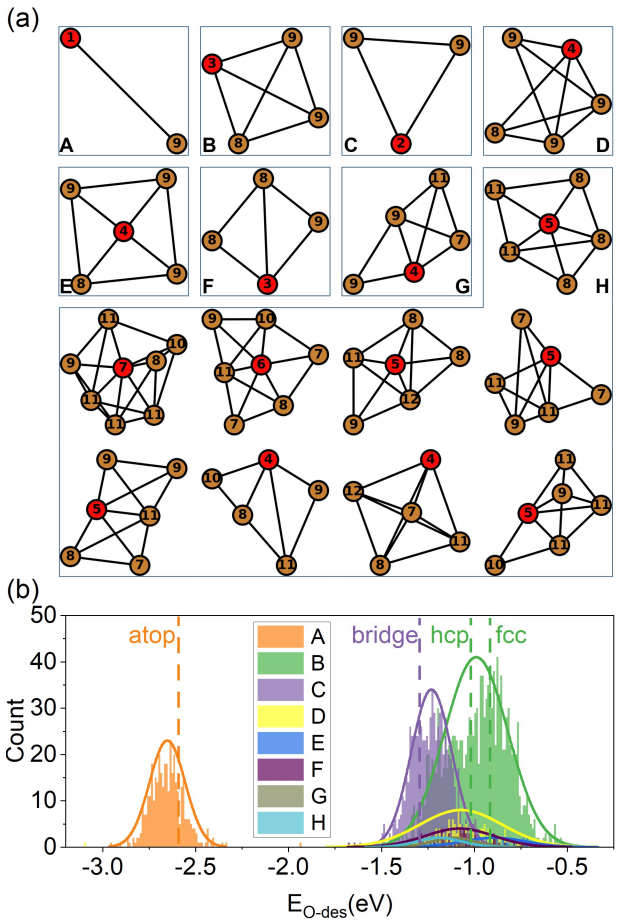

Figure 4. The active sites determined *via* graph theory and the distribution of oxygen desorption

energy. (a) The graph representation of oxygen (red) and its first neighbor copper atoms(brown), the number is a coordinate number, (b) the distribution of oxygen desorption energy for different type of active sites at pH 0 and $U = 0$ V_{SHE}, the solid curves show the Gaussian distribution, and the dashed lines are the desorption energies of oxygen on corresponding active sites on Cu(111).

Discussion

The computational framework employed here provides a systematic approach for understanding the material changes from bulk to surface during the operando conditions not only from a thermodynamic perspective but also from a kinetic standpoint. The simulations point to an OD-Cu oxygen content at zero electric potential vs SHE highly depends on the pH, Cu_2O is reduced to Cu under strongly acidic conditions, while Cu_2O is stable under strongly basic conditions. Under near neutral conditions at zero electric potential vs SHE, the Cu_2O with specific surface area of 0.146 $Å^{-1}$ retains 15 at.% oxygen. The specific surface area of Cu_2O particle affects the reduction degree, the lower the specific surface area, the higher reduction degree. Depending on the size distribution of the Cu_2O particles, the potential window for simultaneous presence of Cu_2O and Cu surfaces are different. While a strong reduction potential could lead to the complete reduction of Cu_2O, the sluggish kinetics of oxygen diffusion from inside to surface makes the process complete in long time (depending on the size, from minutes to hours) in agreement with experimental observations[38]. Comparing to the most recent experiments, the evidence by grazing incidence XPS can be seen as originated by defect species for O close to the surface and for the interstitial ones, and these configurations were also found in our simulations.

As for the reducing/oxidating processes, our computational result match the experimental values even regarding the timescale of the events.[6] XAS combined to EELS analysis demonstrate the metallic nature of the 7 nm NP after 30 min at –0.8 V_{RHE}. After 1 h the EXAFS of these particles retrieves a coordination number for Cu of 8.1 ± 1.6. As EXAFS corresponds to an average of bulk and surface atoms, the observation means that under steady-state conditions Cu catalyst contains a large fraction of undercoordinated sites. This corresponds to our calculation on the equivalent system for which we find the average coordination number is 9.08 and complete oxygen depletion in 7.3 h. In addition, the small Cu structures (7nm) fully reoxidize after 5 h of air exposure[6] while the larger structures form Cu@Cu_2O shell structures (2 nm oxide shell). This also agree with our computed reoxidation shell of 2.1 nm.

EXAFS analysis show that the removal of oxygens ends up with materials that contain a very large amount of disorder. Electrocatalytic experiments show that the disordered grains were responsible for the undercoordinated sites active in CO_2RR. In air exposure experiments these defects can react with O_2 leading to the spontaneous incorporation of oxygen in the lattice. In our simulations, once O_2 is split, the penetration of O in these disordered layers is rather fast, with the oxidation layer reaching saturation within 0.4 ns.

In conclusion, the structures of OD-Cu during the reduction process under different conditions were systematically studied *via* large-scale molecular dynamics at first-principles accuracy with a neural network potential (error 4.58 meV/atom w.r.t. PBE-D2). The oxygen concentration of the OD-Cu materials is strongly dependent on the history of the sample and the reaction conditions, the higher the pH/potential/specific surface area, the higher the oxygen concentration in the most stable OD-Cu configuration. The oxygen atoms tend to aggregate to form Cu_2O on the surface and inside the bulk to reduce the energy by lowering the formation energy and surface energy instead of being distributed uniformly. For long electrochemical experiments OD-Cu materials reduce to Cu but requires a considerable time to remove all the trapped oxygen. In addition, the highly reconstructed Cu surface leads to a wide distribution of oxygen adsorption energy sites, increasing the probability of stable residual oxygen at strong reduction potentials. These results not only reveal the dynamics of the stable structure of OD-Cu under different experimental conditions but also give an insight into the formation mechanism of the reduction of OD-Cu and the limits for fine-tuning by controlling experimental conditions.

Methods

The DFT simulations were performed using the Vienna Ab Initio Simulation Package (VASP)[65,66] with Perdew-Burke-Ernzerhof (PBE) functional[50] and our refitted DFT-D2 van der Waals parameters[51–53]. For valence electrons, a plane-wave basis set was adopted with an energy cutoff of 450 eV, and the ionic cores were described with the projector augmented-wave (PAW) method. The total energy was converged to an accuracy of 1×10^{-6} eV, and a force tolerance of 0.03 eV/Å was used in all structure optimization. The NNPs were trained *via* multistream extended Kalman filter algorithm using energies and forces. To improve the quality of the NNPs, an expanded dataset was built *via* ***active learning*** using a modified framework based on RuNNerActiveLearn[67,68]. The active learning procedure was stopped when no extrapolation was found in the runs and all energy (force) differences between the

two NNPs are lower than 5 (10) times the RMSE of energy (forces). If the potential is not applicable to the above three systems, the active learning would be launched again, and the temperature of NN-MDs would be increased to increase structural diversity. Further tests regarding temperature stability and melting point are presented in Section S2. The simulation of Neural Network based Molecular Dynamic (NN-MD) were performed using LAMMPS code[56] with the NNP interface from n2p2[55,57], For ***equilibrium***, the simulations were run for 1 ns at the indicated temperature. For ***annealing***, the simulations were run at 700 K for 1ns, then the systems were cooled to 300K in 1 ns, and finally another 1 ns for equilibrium at 300 K. The canonical (NVT) ensemble simulations were modeled with the Nose-Hoover thermostat for surface systems, and the Nose-Hoover thermostat and barostat were employed for isobaric-isothermic (NPT) ensemble simulations of bulk systems[69].

Data availability

The source of initial dataset, the final dataset, the machine learning potential files, the molecular dynamics trajectories (reconstitution, coexistence, reduction, deposition, diffusion), and the energy minimization of Oxygen adsorption are available in ioChem-BD database[70] (DOI: http://dx.doi.org/10.19061/iochem-bd-6-228).

Competing interests

The authors declare no competing financial interest.

Authors contribution

Z.L. and N.L. conceived this work and designed the simulations. Z.L. performed the calculations. F.D. assisted the analysis of coordination number and applied electric potential, and reviewed and edited the manuscript before submission. All authors contributed writing of the manuscript.

Acknowledgments

This work was funded by the European Union's Horizon Europe research and innovation programme under the Marie Skłodowska-Curie grant agreement No 101064867, the Spanish Ministry of Science and Innovation (Ref. No. PRE2021-097615, PID2021-122516OB-I00, Severo Ochoa Center of Excellence CEX2019-000925-S 10.13039/501100011033). The authors also thank the Barcelona Supercomputing Center (BSC-RES) for providing generous computational resources.

References

1. Birdja, Y. Y. *et al.* Advances and challenges in understanding the electrocatalytic conversion of carbon dioxide to fuels. *Nat. Energy* **4**, 732–745 (2019).
2. Wang, G. *et al.* Electrocatalysis for CO_2 conversion: from fundamentals to value-added products. *Chem. Soc. Rev.* **50**, 4993–5061 (2021).
3. Das, S. *et al.* Core-shell structured catalysts for thermocatalytic, photocatalytic, and electrocatalytic conversion of CO_2. *Chem. Soc. Rev.* **49**, 2937–3004 (2020).
4. Hori, Y., Murata, A. & Takahashi, R. Formation of hydrocarbons in the electrochemical reduction of carbon dioxide at a copper electrode in aqueous solution. *J. Chem. Soc. Faraday Trans. 1* **85**, 2309–2326 (1989).

5. Zhou, Y. *et al.* Long-chain hydrocarbons by CO_2 electroreduction using polarized nickel catalysts. *Nat. Catal.* **5**, 545–554 (2022).

6. Yang, Y. *et al.* Operando studies reveal active Cu nanograins for CO_2 electroreduction. *Nature* **614**, 262–269 (2023).

7. Ma, M., Djanashvili, K. & Smith, W. A. Controllable Hydrocarbon Formation from the Electrochemical Reduction of CO_2 over Cu Nanowire Arrays. *Angew. Chem. Int. Ed.* **55**, 6680–6684 (2016).

8. Varela, A. S., Kroschel, M., Reier, T. & Strasser, P. Controlling the selectivity of CO_2 electroreduction on copper: The effect of the electrolyte concentration and the importance of the local pH. *Catal. Today* **260**, 8–13 (2016).

9. Pander, J. E. *et al.* Understanding the Heterogeneous Electrocatalytic Reduction of Carbon Dioxide on Oxide-Derived Catalysts. *ChemElectroChem* **5**, 219–237 (2018).

10. Ma, S. *et al.* One-step electrosynthesis of ethylene and ethanol from CO_2 in an alkaline electrolyzer. *J. Power Sources* **301**, 219–228 (2016).

11. Kas, R. *et al.* Electrochemical CO_2 reduction on Cu_2O-derived copper nanoparticles: Controlling the catalytic selectivity of hydrocarbons. *Phys. Chem. Chem. Phys.* **16**, 12194–12201 (2014).

12. Nitopi, S. *et al.* Progress and Perspectives of Electrochemical CO_2 Reduction on Copper in Aqueous Electrolyte. *Chem. Rev.* **119**, 7610–7672 (2019).

13. Bagger, A., Ju, W., Varela, A. S., Strasser, P. & Rossmeisl, J. Electrochemical CO_2 Reduction: Classifying Cu Facets. *ACS Catal.* **9**, 7894–7899 (2019).

14. Dattila, F., García-Muelas, R. & López, N. Active and Selective Ensembles in Oxide-Derived Copper Catalysts for CO_2 Reduction. *ACS Energy Lett.* **5**, 3176–3184 (2020).

15. Lin, S. C. *et al.* Operando time-resolved X-ray absorption spectroscopy reveals the chemical nature enabling highly selective CO_2 reduction. *Nat. Commun.* **11**, 1–12 (2020).

16. Arán-Ais, R. M., Scholten, F., Kunze, S., Rizo, R. & Roldan Cuenya, B. The role of in situ generated morphological motifs and Cu(I) species in C_{2+} product selectivity during CO_2 pulsed electroreduction. *Nat. Energy* **5**, 317–325 (2020).

17. Zhou, Y. *et al.* Dopant-induced electron localization drives CO_2 reduction to C_2 hydrocarbons. *Nat. Chem.* **10**, 974–980 (2018).

18. Jeong, H. M. *et al.* Atomic-Scale Spacing between Copper Facets for the Electrochemical

Reduction of Carbon Dioxide. *Adv. Energy Mater.* **10**, 1–12 (2020).

19. Gao, D., Aran-Ais, R. M., Jeon, H. S. & Roldan Cuenya, B. Rational catalyst and electrolyte design for CO_2 electroreduction towards multicarbon products. *Nat. Catal.* **2**, 198–210 (2019).
20. Li, C. W. & Kanan, M. W. CO_2 reduction at low overpotential on Cu electrodes resulting from the reduction of thick Cu_2O films. *J. Am. Chem. Soc.* **134**, 7231–7234 (2012).
21. Zhu, C. *et al.* Product-Specific Active Site Motifs of Cu for Electrochemical CO_2 Reduction. *Chem* **7**, 406–420 (2021).
22. Lum, Y. & Ager, J. W. Evidence for product-specific active sites on oxide-derived Cu catalysts for electrochemical CO_2 reduction. *Nat. Catal.* **2**, 86–93 (2019).
23. Jiang, K. *et al.* Metal ion cycling of Cu foil for selective C-C coupling in electrochemical CO_2 reduction. *Nat. Catal.* **1**, 111–119 (2018).
24. Kim, D., Kley, C. S., Li, Y. & Yang, P. Copper nanoparticle ensembles for selective electroreduction of CO_2 to C_2–C_3 products. *Proc. Natl. Acad. Sci. U. S. A.* **114**, 10560–10565 (2017).
25. Dutta, A., Rahaman, M., Luedi, N. C., Mohos, M. & Broekmann, P. Morphology Matters: Tuning the Product Distribution of CO_2 Electroreduction on Oxide-Derived Cu Foam Catalysts. *ACS Catal.* **6**, 3804–3814 (2016).
26. Reske, R., Mistry, H., Behafarid, F., Roldan Cuenya, B. & Strasser, P. Particle size effects in the catalytic electroreduction of CO_2 on Cu nanoparticles. *J. Am. Chem. Soc.* **136**, 6978–6986 (2014).
27. Loiudice, A. *et al.* Tailoring Copper Nanocrystals towards C_2 Products in Electrochemical CO_2 Reduction. *Angew. Chem. Int. Ed.* **55**, 5789–5792 (2016).
28. Kim, D., Resasco, J., Yu, Y., Asiri, A. M. & Yang, P. Synergistic geometric and electronic effects for electrochemical reduction of carbon dioxide using gold-copper bimetallic nanoparticles. *Nat. Commun.* **5**, 1–8 (2014).
29. Wang, H. *et al.* Direct Evidence of Subsurface Oxygen Formation in Oxide-Derived Cu by X-ray Photoelectron Spectroscopy. *Angew. Chem. Int. Ed.* **61**, e202111021 (2022).
30. Velasco-Velez, J. J. *et al.* Revealing the Active Phase of Copper during the Electroreduction of CO_2 in Aqueous Electrolyte by Correlating in Situ X-ray Spectroscopy and in Situ Electron Microscopy. *ACS Energy Lett.* **5**, 2106–2111 (2020).
31. Ren, D. *et al.* Selective Electrochemical Reduction of Carbon Dioxide to Ethylene and Ethanol

on Copper(I) oxide catalysts. *ACS Catal.* **5**, 2814–2821 (2015).

32. Lum, Y. & Ager, J. W. Stability of Residual Oxides in Oxide-Derived Copper Catalysts for Electrochemical CO_2 Reduction Investigated with ^{18}O Labeling. *Angew. Chem. Int. Ed.* **57**, 551–554 (2018).
33. Garza, A. J., Bell, A. T. & Head-Gordon, M. Is Subsurface Oxygen Necessary for the Electrochemical Reduction of CO_2 on Copper? *J. Phys. Chem. Lett.* **9**, 601–606 (2018).
34. Fields, M., Hong, X., Nørskov, J. K. & Chan, K. Role of Subsurface Oxygen on Cu Surfaces for CO_2 Electrochemical Reduction. *J. Phys. Chem. C* **122**, 16209–16215 (2018).
35. Chen, C. *et al.* The in situ study of surface species and structures of oxide-derived copper catalysts for electrochemical CO_2 reduction. *Chem. Sci.* **12**, 5938–5943 (2021).
36. Lee, S. H. *et al.* Oxidation State and Surface Reconstruction of Cu under CO_2 Reduction Conditions from in Situ X-ray Characterization. *J. Am. Chem. Soc.* **143**, 588–592 (2021).
37. Jung, H. *et al.* Electrochemical Fragmentation of Cu_2O Nanoparticles Enhancing Selective C-C Coupling from CO_2 Reduction Reaction. *J. Am. Chem. Soc.* **141**, 4624–4633 (2019).
38. Timoshenko, J. *et al.* Steering the structure and selectivity of CO_2 electroreduction catalysts by potential pulses. *Nat. Catal.* **5**, 259–267 (2022).
39. Chen, J. & Wang, L. Effects of the Catalyst Dynamic Changes and Influence of the Reaction Environment on the Performance of Electrochemical CO_2 Reduction. *Adv. Mater.* **34**, 2103900 (2021).
40. Dattila, F., Seemakurthi, R. R., Zhou, Y. & López, N. Modeling Operando Electrochemical CO_2 Reduction. *Chem. Rev.* **122**, 11085–11130 (2022).
41. Mandal, L. *et al.* Investigating the Role of Copper Oxide in Electrochemical CO_2 Reduction in Real Time. *ACS Appl. Mater. Interfaces* **10**, 8574–8584 (2018).
42. Scott, S. B. *et al.* Absence of Oxidized Phases in Cu under CO Reduction Conditions. *ACS Energy Lett.* **4**, 803–804 (2019).
43. Beverskog, B. & Puigdomenech, I. Revised Pourbaix Diagrams for Copper at 25 to 300°C. *J. Electrochem. Soc.* **144**, 3476–3483 (1997).
44. Favaro, M. *et al.* Subsurface oxide plays a critical role in CO_2 activation by Cu(111) surfaces to form chemisorbed CO_2, the first step in reduction of CO_2. *Proc. Natl. Acad. Sci. U. S. A.* **114**, 6706–6711 (2017).
45. Eilert, A. *et al.* Subsurface Oxygen in Oxide-Derived Copper Electrocatalysts for Carbon

Dioxide Reduction. *J. Phys. Chem. Lett.* **8**, 285–290 (2017).

46. He, M. *et al.* Oxygen induced promotion of electrochemical reduction of CO_2 via co-electrolysis. *Nat. Commun.* **11**, 1–10 (2020).

47. Liu, G. *et al.* CO_2 reduction on pure Cu produces only H_2 after subsurface O is depleted: Theory and experiment. *Proc. Natl. Acad. Sci. U. S. A.* **118**, e2012649118 (2021).

48. Gauthier, J. A., Stenlid, J. H., Abild-Pedersen, F., Head-Gordon, M. & Bell, A. T. The Role of Roughening to Enhance Selectivity to C_{2+} Products during CO_2 Electroreduction on Copper. *ACS Energy Lett.* **6**, 3252–3260 (2021).

49. Cheng, D. *et al.* The nature of active sites for carbon dioxide electroreduction over oxide-derived copper catalysts. *Nat. Commun.* **12**, 1–8 (2021).

50. Perdew, J. P., Burke, K. & Ernzerhof, M. Generalized Gradient Approximation Made Simple. *Phys. Rev. Lett.* **77**, 3865–3868 (1996).

51. Grimme, S. Semiempirical GGA-type density functional constructed with a long-range dispersion correction. *J. Comput. Chem.* **27**, 1787–1799 (2006).

52. Bučko, T., Hafner, J., Lebègue, S. & Ángyán, J. G. Improved description of the structure of molecular and layered crystals: Ab initio DFT calculations with van der Waals corrections. *J. Phys. Chem. A* **114**, 11814–11824 (2010).

53. Almora-Barrios, N., Carchini, G., Błoński, P. & López, N. Costless derivation of dispersion coefficients for metal surfaces. *J. Chem. Theory Comput.* **10**, 5002–5009 (2014).

54. Behler, J. Atom-centered symmetry functions for constructing high-dimensional neural network potentials. *J. Chem. Phys.* **134**, 074106 (2011).

55. Singraber, A., Morawietz, T., Behler, J. & Dellago, C. Parallel Multistream Training of High-Dimensional Neural Network Potentials. *J. Chem. Theory Comput.* **15**, 3075–3092 (2019).

56. Thompson, A. P. *et al.* LAMMPS - a flexible simulation tool for particle-based materials modeling at the atomic, meso, and continuum scales. *Comput. Phys. Commun.* **271**, 108171 (2022).

57. Singraber, A., Behler, J. & Dellago, C. Library-Based LAMMPS Implementation of High-Dimensional Neural Network Potentials. *J. Chem. Theory Comput.* **15**, 1827–1840 (2019).

58. Behler, J. Four Generations of High-Dimensional Neural Network Potentials. *Chem. Rev.* **121**, 10037–10072 (2021).

59. Nørskov, J. K. *et al.* Origin of the Overpotential for Oxygen Reduction at a Fuel-Cell Cathode.

J. Phys. Chem. B **108**, 17886–17892 (2004).

60. García de Arquer, F. P. *et al.* CO_2 electrolysis to multicarbon products at activities greater than 1 A cm^{-2}. *Science* **367**, 661–666 (2020).

61. Jain, A. *et al.* Commentary: The materials project: A materials genome approach to accelerating materials innovation. *APL Mater.* **1**, 011002 (2013).

62. Maginn, E. J., Messerly, R. A., Carlson, D. J., Roe, D. R. & Elliot, J. R. Best Practices for Computing Transport Properties 1. Self-Diffusivity and Viscosity from Equilibrium Molecular Dynamics [Article v1.0]. *Living J. Comput. Mol. Sci.* **2**, 1–20 (2020).

63. Ong, S. P. *et al.* Python Materials Genomics (pymatgen): A robust, open-source python library for materials analysis. *Comput. Mater. Sci.* **68**, 314–319 (2013).

64. Deshpande, S., Maxson, T. & Greeley, J. Graph theory approach to determine configurations of multidentate and high coverage adsorbates for heterogeneous catalysis. *npj Comput. Mater.* **6**, 79 (2020).

65. Kresse, G. & Furthmuller, J. Efficient iterative schemes for ab initio total-energy calculations using a plane-wave basis set. *Phys. Rev. B* **54**, 11169–11186 (1996).

66. Kresse, G. & Furthmuller, J. Efficiency of ab-initio total energy calculations for metals and semiconductors using a plane-wave basis set. *Comput. Mater. Sci.* **6**, 15–50 (1996).

67. Eckhoff, M. & Behler, J. From Molecular Fragments to the Bulk: Development of a Neural Network Potential for MOF-5. *J. Chem. Theory Comput.* **15**, 3793–3809 (2019).

68. Eckhoff, M. & Behler, J. High-dimensional neural network potentials for magnetic systems using spin-dependent atom-centered symmetry functions. *npj Comput. Mater.* **7**, 1–11 (2021).

69. Frenkel, D. & Smit, B. Understanding Molecular Simulation. *Academic Press* (2002).

70. Álvarez-Moreno, M. *et al.* Managing the Computational Chemistry Big Data Problem: The ioChem-BD Platform. *J. Chem. Inf. Model.* **55**, 95–103 (2015).